



Nanoscale

Shear-induced liquid-crystalline phase transition behaviour of colloidal solutions of hydroxyapatite nanorod composites

Journal:	<i>Nanoscale</i>
Manuscript ID	NR-ART-12-2019-010996.R1
Article Type:	Paper
Date Submitted by the Author:	18-Feb-2020
Complete List of Authors:	<p>Kajiyama, Satoshi; University of Tokyo, Department of Chemistry and Biotechnology Iwase, Hiroki; Comprehensive Research Organization for Science and Society (CROSS), Research Center for Neutron Science & Technology Nakayama, Masanari; The University of Tokyo, Department of Chemistry and Biotechnology, School of Engineering Ichikawa, Rino; University of Tokyo, Department of Chemistry and Biotechnology Yamaguchi, Daisuke; The University of Tokyo, Seto, Hideki; High Energy Accelerator Research Organization, Institute of Materials Structure Science Kato, Takashi; University of Tokyo, Chemistry and Biochemistry</p>

SCHOLARONE™
Manuscripts

ARTICLE

Shear-induced liquid-crystalline phase transition behaviour of colloidal solutions of hydroxyapatite nanorod composites

Satoshi Kajiyama,^a Hiroki Iwase,^b Masanari Nakayama,^a Rino Ichikawa,^a Daisuke Yamaguchi,^a Hideki Seto,^{*c} and Takashi Kato^{*a}

Received 00th January 20xx,
Accepted 00th January 20xx

DOI: 10.1039/x0xx00000x

Liquid-crystalline (LC) bio-inspired materials based on colloidal nanoparticles with anisotropic morphologies such as sheets, plates, rods and fibers, were found for functional materials. They show stimuli-responsive behaviour by mechanical force and in electric, and magnetic fields. Understanding of effects of external stimuli on structures of anisotropic colloidal particles is important for the development of highly ordered structures. Recently, we developed stimuli-responsive hydroxyapatite (HAP)-based colloidal LC nanorods that are candidates as environmentally-friendly functional materials. In the present study, ordering behaviour of HAP nanorod dispersions, which show LC states, has been examined with *in-situ* small-angle neutron scattering and rheological measurements (Rheo-SANS) under shearing force. The structural analyses and dynamic viscosity observations provide the detail information about the effects of shear force on the structural change of HAP nanorods in D₂O dispersion. The present Rheo-SANS measurements unraveled three kinds of main effects of the shear force; the enhancement of interactions between HAP nanorods, alignment of HAP nanorods to the shear flow direction, and the formation and disruption of HAP nanorod assemblies. Simultaneous analyses of dynamic viscosity and structural changes revealed that the HAP nanorod dispersions exhibited distinctive rheological properties accompanying with their ordered structural change.

Introduction

Colloidal particle dispersions are found in nature as sediments and muds, and they have been also utilized in a wide variety of fields including daily use in petroleum, paint, cosmetic, and concrete industries.^{1,2} In these natural and engineered contexts, the flow behaviour of colloidal dispersions is often of central interests, as it may determine the processability in transportations and applications.^{1–12} In particular, colloidal dispersions of rod particles have fluidic anisotropic properties that potentially induce a drastic change in rheological or hydrodynamic properties from conventional sphere colloidal particles, but they have been rarely studied.^{8–12} Colloidal rod particles show liquid-crystalline (LC) phases in a certain range of concentrations, and their orientation in LC states can be controlled with mechanical shear force.^{13–19} Macroscopically aligned LC colloidal materials with external stimuli including mechanical shear force have been studied towards a variety of applications in biomaterials, high strength materials, optical

materials, actuators and sensors.^{13–27} It is still a challenging issue to understand the dynamics of structural change of colloidal LC materials based on rod particles with shear force.

Recently, we achieved the successful synthesis of LC colloidal nanorods based on hydroxyapatite (HAP)¹³ and CaCO₃¹⁴ through an approach inspired by biomineralization. The recent development of LC HAP colloidal dispersions¹³ enables us to control HAP ordered structures in macroscales by mechanical shear force. HAP is an environmentally-friendly resources having potentials of applications to a wide variety of fields as cell scaffolds²¹, catalysts²⁸, absorbents²⁹, structural materials³⁰, optical materials^{13,31}, and dielectric materials^{32,33}. Because these properties significantly depend on the crystallographic orientation of HAP crystals, numerous efforts have been devoted to control its crystallographic orientation.^{13,21,34–39} Among these techniques for alignment control of HAP-based assemblies, the shear force alignment is a particularly useful method because it does not require special equipments and treatments.¹³ Understanding of ordering behaviour of HAP nanorods in LC states is important for construction of HAP-based materials with highly ordered structures that enhance functionalities.

Here our objective is to observe ordering behaviour of HAP nanorods in LC states with *in-situ* small-angle neutron scattering and rheological (Rheo-SANS) measurements. Rheo-SANS measurements provide information about the structural change of molecular assemblies under mechanical shear force.^{40–46} The Rheo-SANS technique is a powerful tool for the

^a Department of Chemistry and Biotechnology, School of Engineering, The University of Tokyo, 7-3-1 Hongo, Bunkyo-ku, Tokyo 113-8656, Japan. E-mail: kato@chiral.t.u-tokyo.ac.jp

^b Neutron Science and Technology Center, Comprehensive Research Organization for Science and Society (CROSS), 162-1 Shirataka, Tokai, Ibaraki 319-1106, Japan

^c J-PARC Center, High Energy Accelerator Research Organization, 203-1 Shirataka, Tokai, Ibaraki 319-1106, Japan. E-mail: hideki.seto@kek.jp

Electronic Supplementary Information (ESI) available: [details of any supplementary information available should be included here]. See DOI: 10.1039/x0xx00000x

observation of shear-flow-induced structural change accompanying with the change of rheological behaviour, especially for one-dimensional

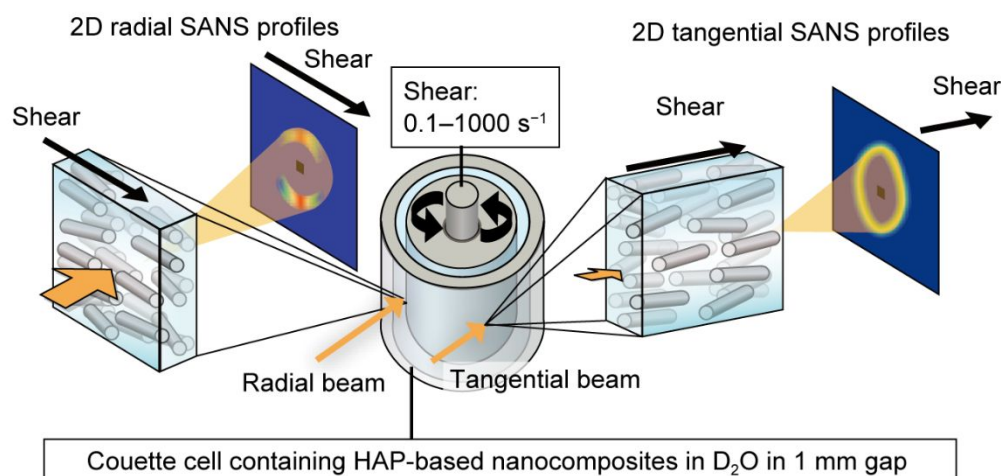


Fig. 1 Schematic illustration of experimental geometries of Rheo-SANS measurements of HAP-based nanocomposites in D_2O solution. Radial and tangential neutron beams provide the structural information in two different geometries.

materials that are aligned parallel to the shear flow direction.^{43–46} However, ordering behaviour of almost LC materials has not been studied with Rheo-SANS measurements, including inorganic colloidal LC nanorods.

In the present study, we have conducted Rheo-SANS measurements on HAP nanorod dispersions with various concentrations in isotropic or LC states in order to clarify the effects of mechanical shear force on ordered structures of HAP-based nanorod composites in D_2O dispersion. Two-dimensional (2D) SANS profiles in the parallel and perpendicular directions to the shear flow provided significant information on the structures of aligned HAP nanorods (Fig. 1). The correlation between their structures and rheological behaviour disclosed unusual phase transition behaviour of the HAP nanorod dispersions.

Experimental methods

All chemical reagents used for the synthesis of HAP crystals were obtained from commercial sources. Calcium chloride ($CaCl_2$) and tripotassium phosphate (K_3PO_4) were obtained from Fujifilm Wako Pure Chemical Corporation Ltd., (Osaka, Japan). Poly(acrylic acid) (PAA, $M_w = 1.8 \times 10^3$) and deuterium oxide (D_2O , 99%) was purchased from Sigma-Aldrich (St Louis, MO, USA). All chemicals were used as received without further purification.

HAP-based nanorod composites showing an LC behaviour were synthesized in accordance with previously reported procedures.¹³ A $CaCl_2$ (100 mM) aqueous solution containing PAA ($M_w = 2.0 \times 10^3$, 7.2×10^{-1} wt%) was mixed with an equal volume of a K_3PO_4 (100 mM) aqueous solution. The mixed solution was stirred for 1 day at $60^\circ C$ and then centrifuged. The supernatant was decanted. The collected precipitates

were washed using purified water and centrifuged. Then, the sediments were washed with D_2O at twice to exchange the solvent to D_2O . The HAP nanorods in D_2O dispersion were obtained with dilution of the sediments with D_2O after centrifugation.

A rheometer (Anton Paar MCR302) (Graz, Austria) was set up at the small- and wide-angle neutron scattering instrument (TAIKAN) installed on the BL15 beamline at Materials and Life Science Experimental Facility (MLF) in Japan Proton Accelerator Research Complex (J-PARC). A double-cylinder-type (Couette) cell of quartz glass inner rotor with $20\text{ mm}\Phi$ and quartz glass outer stable cylinder with $22\text{ mm}\Phi$ of inner diameter was employed, as shown in Fig. 2. Information of SANS both radial, using $10\text{ mm}\Phi$ neutron beam, and tangential, using a $0.5\text{ mm}\times 10\text{ mm}$ beam, were collected in the static colloidal solution states without shear rate, and with shear rate of $0.1\text{--}1000\text{ s}^{-1}$ at $30^\circ C$. The measurement temperature is controlled with a gas flow. Using the pulsed neutrons in the wide range of wavelength ($\lambda = 0.1\text{--}0.78\text{ nm}$) based on a time-of-flight method and four area detector banks, TAIKAN can cover a wide Q -range from 5×10^{-2} to 150 nm^{-1} simultaneously, where the magnitude of the scattering vector Q is defined by $Q = 4\pi\sin(\theta/2)/\lambda$, where λ and θ represent the wavelength and the scattering angle, respectively. This Q -range corresponds to $0.004\text{ nm} < d < 125\text{ nm}$ in real space. The observed Q range was limited to $5\times 10^{-2}\text{ nm}^{-1} < Q < 50\text{ nm}^{-1}$, corresponding to $0.1\text{ nm} < d < 125\text{ nm}$ in real space, due to an increasing background level by incoherent scattering from hydrogen atoms in a higher Q range. The SANS data were collected from D_2O suspensions in the rheometer under the shear rate at 0 s^{-1} (static) and $0.1\text{--}1000\text{ s}^{-1}$ by the radial or tangential geometry. Background spectra in radial and tangential geometries were recorded

using D₂O solvent in the couette cell. The absolute SANS intensity was obtained by using a secondary standard of glassy carbon.⁴⁷ The radial and tangential geometry observations offer us the structural information parallel and perpendicular to the shear direction, respectively.

Thermogravimetric (TG) measurements of HAP nanorod dispersions were performed up to 1000°C at a heating rate of 10 °C min⁻¹ under air flow (100 mL min⁻¹) using a TG-8120 (Rigaku, Tokyo, Japan), in order to measure the concentration of HAP nanorods in D₂O dispersion. Optical properties of the HAP nanorod dispersions were investigated using a polarizing optical microscope (BX51, Olympus Co., Tokyo, Japan). For transmission electron microscopy (TEM) observation, hydroxyapatite-based nanocomposites were located on Cu microgrids with a 100 mesh. TEM characterization was performed using a JEM-2800 (JEOL, Tokyo, Japan) operated at 100 kV.

Results and discussion

Analyses of 2D SANS profiles

Morphologies of HAP nanorods that were obtained through previously reported procedure¹³ were observed with transmission electron microscopy (TEM) (Fig. 2). Mean size of HAP nanorods was *ca.* 100 nm in length and *ca.* 20 nm in width, respectively (Fig. 2a). TEM observation revealed that one HAP nanorod was not a single crystal but an assembly of nanorod crystallites 20–40 nm in length and 5 nm in width (Fig. 2b,c). To observe the LC behaviour of the HAP nanorod colloidal dispersions in D₂O, the concentration of HAP nanorod dispersion was adjusted to 3.3, 4.4, 6.7, 8.7, and 9.7 vol%. On

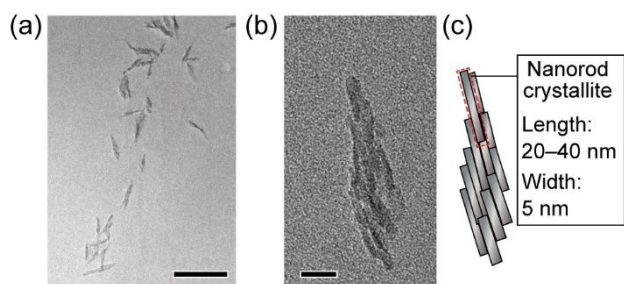


Fig. 2 (a) TEM images for HAP-based nanorod composites (Scale bar: 100 nm). (b) High-magnified TEM image showing nanocrystallites with 20–40 nm length and *ca.* 5 nm width (Scale bar: 20 nm). (c) Schematic illustration of HAP-based nanorods composed of nanocrystallites.

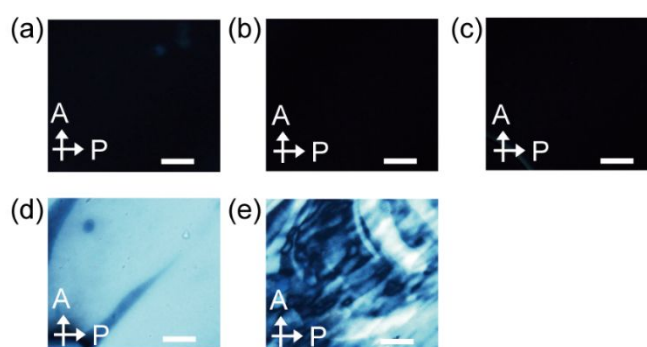


Fig. 3 Polarizing optical microscope images of colloidal HAP nanorod composites in D₂O solution with various concentrations; (a) 3.3, (b) 4.4, (c) 6.7, (d) 8.7 and (e) 9.7 vol%. Scale bar: 100 μm, A: analyzer, P: polarizer.

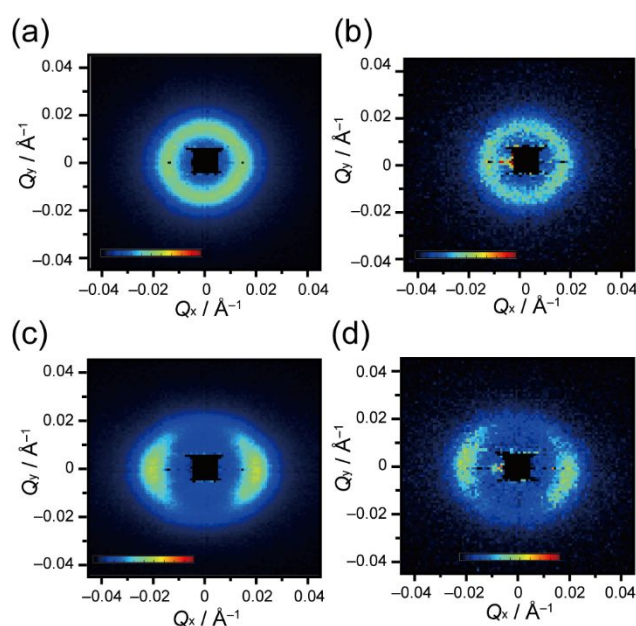


Fig. 4 Representative (a,c) radial and (b,d) tangential 2D SANS profiles of HAP nanorod composite dispersions without shear rates in (a,b) isotropic (4.4 vol%) and (c,d) LC (8.7 vol%) states.

the basis of polarizing optical microscopy (POM) observations, the dispersions with 3.3 – 6.7 vol% were isotropic phases, while HAP nanorod dispersions with 8.7 and 9.7 vol% were LC phases (Fig. 3).

Static structures of HAP nanorods were examined with SANS measurements without mechanically shear force. For 3.3 – 6.7 vol%, 2D SANS profiles were isotropic in both radial and tangential directions (Fig. 4a,b and Fig. S2–S7), while 8.7 and 9.7 vol% HAP nanorod dispersions showed anisotropic 2D SANS profiles in the radial direction (Fig. 4c,d and Fig. S8–S11). In LC states of 8.7 and 9.7 vol% HAP dispersions, the HAP nanorods were aligned under shear force during sample setting into the 1-mm-gap couette quartz cell.

To evaluate the isotropic static structures without shear force, the observed results of Rheo-SANS measurements were fitted with simulated patterns. The scattering intensity functions for nanorod is given by

$$I(Q) = (\Delta\rho)^2 n V^2 P(Q) S(Q) \quad (1)$$

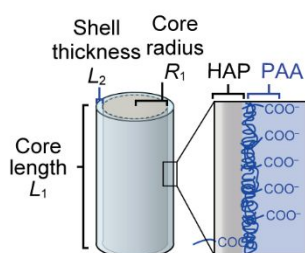
where $\Delta\rho$ is the scattering contrast, n and V are the number density and the volume of nanorods, respectively, $P(Q)$ is the form factor, and $S(Q)$ is the structure factor. For the simulation of $P(Q)$ and $S(Q)$, we used simple models of HAP nanorod or ellipsoid dispersions as shown in Fig. 5. No significant difference was observed in simulated SANS profiles between nanorod and ellipsoid models of HAP morphologies for the simulation $P(Q)$. Therefore, only simulation results with a HAP nanorod model are shown in the present study. $P(Q)$ for rod particles with a cross-sectional radius R_c and length L oriented by the angle β with respect to the reference axis is given by⁴³

where $J_1(x)$ is the first-order Bessel function of x . The model of randomly oriented rod particles was used for fitting of simulated SANS profiles with averaged SANS curves in radial directions of 3.3–6.7 vol% HAP nanorod dispersions, where 2D SANS profiles were observed as ring patterns (Fig. S2–S7). For the randomly orientation, the form factor is given by

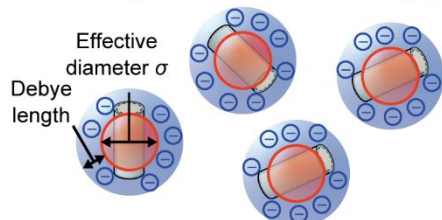
$$P_{rod}(Q) = \int_0^{\pi/2} \left[\frac{2J_1(QR_c \sin \beta)}{(QR_c \sin \beta)^2} \frac{\sin(Q(L/2) \cos \beta)}{Q(L/2) \cos \beta} \right]^2 \sin \beta d\beta \quad (3)$$

Taking into account the composite nanostructures of HAP-based nanorods,¹³ a core-shell model comprising a HAP nanorod covered with PAA was applied for the simulation of form factor $P(Q)$ (Fig. 5a). In the diluted system without interparticle interactions, the structure factor $S(Q)$ is considered to be 1. In this case, the SANS profiles that were

(a) PAA/HAP core-shell nanorod model for $P(Q)$



(b) Surface-charged colloid model for $S(Q)$



(c) Paracrystal model for $S(Q)$

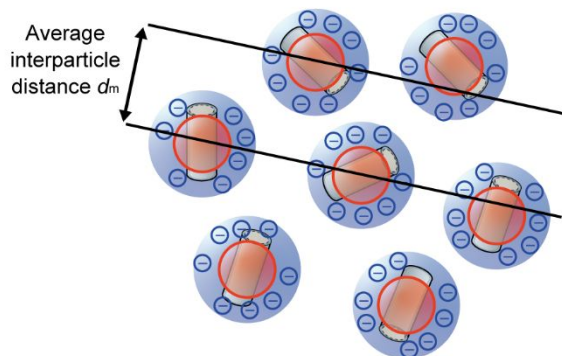


Fig. 5 Schematic illustration of used structural models for simulation of SANS profiles. (a) Core-shell nanorod model of HAP-based nanocomposites for simulation of $P(Q)$. (b) Surface-charged colloid model for simulation of $S(Q)$. (c) Paracrystal model for simulation of $S(Q)$.

$$P_{rod}(Q, \beta) = \left[\frac{2J_1(QR_c \sin \beta)}{(QR_c \sin \beta)^2} \frac{\sin(Q(L/2) \cos \beta)}{Q(L/2) \cos \beta} \right]^2 \quad (2)$$

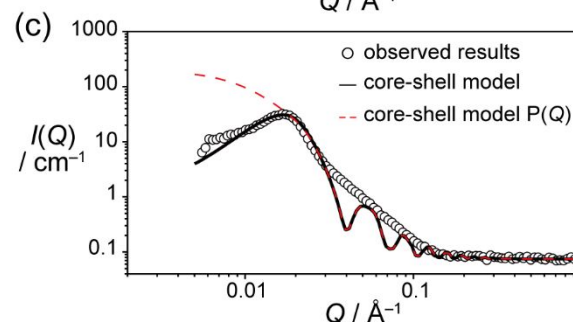
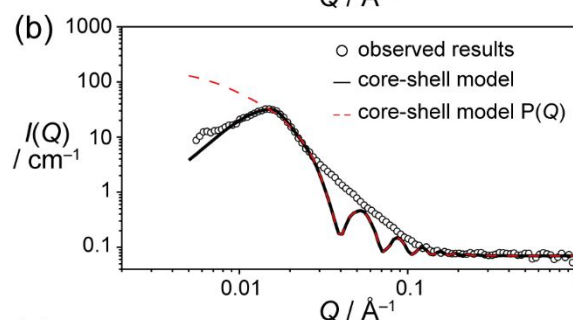
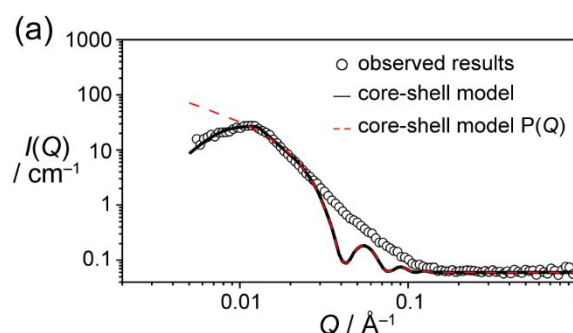


Fig. 6 Fitting results of sector-averaged SANS curves of (a) 3.3, (b) 4.4, and (c) 6.7 vol% HAP nanorod dispersions without shear force. The core-shell nanorod model and surface charge colloid model were used for simulation of $P(Q)$ and $S(Q)$, respectively. White circle: observed curve; black line: simulated curve considering $P(Q)$ and $S(Q)$; red line: simulated $P(Q)$ curve with a core-shell model.

Table 1 Parameters for the production of simulated SANS profiles with a core-shell rod-

Parameter	Volume fraction		
	3.3vol%	4.4vol%	6.7vol%
Core radius R_1 (\AA) ^a	82.23	82.23	82.23
Core length L_1 (\AA) ^c	993.3	668.41	518.8
Core contrast $\Delta\rho_1$ (\AA^{-2}) ^a	-1.27×10^{-6}	-1.27×10^{-6}	-1.27×10^{-6}
Shell thickness L_2 (\AA) ^b	13.04	9.42	9.42
Shell contrast $\Delta\rho_2$ (\AA^{-2}) ^b	-0.95×10^{-6}	-2.53×10^{-6}	-2.53×10^{-6}
Debye length (\AA) ^b	374.7	287.6	265.2
Effective diameter σ (\AA) ^b	210.6	174.6	162.1
Background (cm^{-1}) ^b	0.06	0.07	0.075

particle model for $P(Q)$ and a surface-charged colloid model for $S(Q)$

For the simulation of SANS profiles, temperature, dielectric constant of solvent, and molecular weight is constant as 303 (K), 78 (-), and 1000 (g mol^{-1}), respectively

^a Considered to be constant parameters upon the curve fitting.

^b Considered to be variable parameters upon the curve fitting.

^c Considered to be a constant parameter, but varied for curve fitting.

simulated with a core-shell model $P(Q)$ did not show any peaks in the Q region $0.011 - 0.022 \text{ \AA}^{-1}$, shown as dotted red line in Fig. 6. SANS Simulated $P(Q)$ supported the assumption that HAP nanorod particles have specific interactions each other. For the simulation of structure factor $S(Q)$, the function for ionic surfactant micelles interacting through a repulsive screened Coulomb potential⁴⁵ was applied because the colloidal states of HAP nanorods were stabilized by the electrostatic repulsion force of negative surface charge,¹³ which is derived from PAA on the surface of HAP nanorods (Fig. 5b). Therefore, structure factor $S(Q)$ was given by

$$S(Q) = \frac{1}{1 - 24\phi a(Q\sigma)} \quad (4)$$

where ϕ is the volume fraction, σ is the effective particle diameter, and the $a(Q\sigma)$ was analytically given by Hayter and Penfold,⁴⁸ and depended on both the volume fraction and the Debye length. Using the form factor of equation (3) and structure factor of equation (4), the fitting with observed SANS curves were performed (Fig. 6). The simulated curves explained the observed profiles at $Q < 0.025 \text{ \AA}^{-1}$.

The fitted parameters using the model of the HAP/PAA core-shell structures are shown in Table 1. Background parameters were set to be fitted with the $Q > 0.1 \text{ \AA}^{-1}$ region, where only incoherent scattering was observed. Upon the fitting, core contrast $\Delta\rho_1$ values were underestimated, which may be caused by the irregular shape of HAP-based rod particles as well as nanocrystalline features. Determination of precise chemical composition is difficult for nanosized HAP particles because defective HAP structures are easily formed,⁴⁹ thereby the simulation of SANS profiles were conducted with the core contrast $\Delta\rho_1$ value of $-1.27 \times 10^{-6} \text{ \AA}^{-2}$. Additionally, scattering contrast $\Delta\rho_2$ in the region of PAA shell is also variable because of the swollen properties of PAA.⁵⁰⁻⁵² In D_2O

dispersion, PAA surface accommodated D_2O molecules, resulting in decrease of absolute values of the shell contrast $\Delta\rho_2$ and increase of shell thickness L_2 . Parameters for effective diameter σ and Debye length represented the interparticle interaction force. These changes suggest a fact that the repulsion force among particles was reduced with increasing the concentration (Table 1). However, for fitting of simulated SANS curves with experimental results, core length L_1 was needed to be decreased with increasing the concentration (Table 1). These results suggest that the interactions among HAP nanorods were not only local and isotropic forces such as van der Waals interactions and electrostatic repulsion forces. In dense solution, colloidal particles have a variety of interactions in short and long-range order, even in the case of spherical colloidal particles.¹⁻⁸ As for rod particles, Brownian rotation motion generate a particular repulsion force among particles, such as steric repulsion or excluded volume effects. In the present study, these interactions should be considered in order to simulate SANS profiles with a model based on particle interactions.

Because the interaction among HAP nanorods is too complicated to be defined, another model called as the Hosemann paracrystal model was used for the calculation of

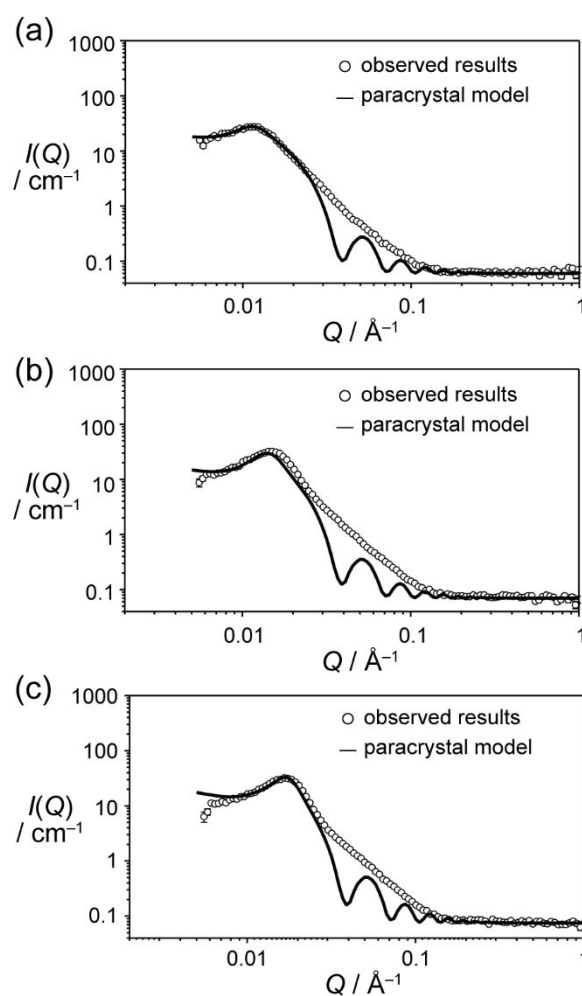


Fig. 7 Fitting results of sector-averaged SANS intensity curve of (a) 3.3, (b) 4.4 and (c) 6.7 vol% HAP nanorod dispersions without shear force using $S(Q)$ of Hosemann paracrystal model. white circle: observed profile; black line: fitted curves.

Table 2 Parameters for the production of simulated SANS profiles with a core-shell rod-particle model for $P(Q)$ and Hosemann paracrystal model for $S(Q)$

Parameter	Volume fraction		
	3.3vol%	4.4vol%	6.7vol%
Core radius R_1 (Å) ^a	82.23	82.23	82.23
Core length L_1 (Å) ^a	934.7	934.7	934.7
Core contrast $\Delta\rho_1$ (Å ⁻²) ^a	-1.27×10^{-6}	-1.27×10^{-6}	-1.27×10^{-6}
Shell thickness L_2 (Å) ^b	9.31	9.31	9.31
Shell contrast $\Delta\rho_2$ (Å ⁻²) ^b	-2.81×10^{-6}	-2.81×10^{-6}	-2.81×10^{-6}
Interparticle distance d_m (Å) ^b	431.3	380.4	323.6
Dispersion of distance w (-) ^b	0.404	0.330	0.304
Background (cm ⁻¹) ^b	0.06	0.07	0.075

For the simulation of SANS profiles, temperature, dielectric constant of solvent, and molecular weight is constant as 303 K, 78 (-), and 1000 (g mol⁻¹), respectively

^a Considered to be constant parameters upon the curve fitting.

^b Considered to be variable parameters upon the curve fitting.

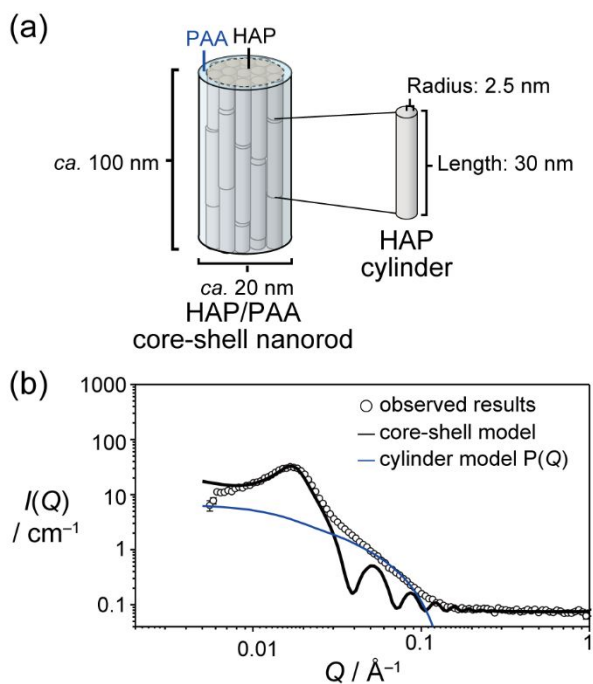


Fig. 8 (a) Schematic illustration of cylinder model for HAP-based nanorods. (b) Fitting results of averaged SANS profiles of 6.7 vol% HAP nanorod dispersions. white circle: observed profile; black line: fitted curves; blue line: cylinder model $P(Q)$.

Table 3 Parameters for fitting of SANS profiles with a cylinder model in the Q region 0.05–0.1 Å⁻¹.

Parameter ^a	
Radius (Å)	25
Length (Å)	300
Contrast (Å ⁻²)	-1.27×10^{-6}
Scale factor (-)	0.07

^a Determined with the TEM observation results as shown in Fig. 2.

structure factor (Fig. 5c).⁵³ Hosemann paracrystal model is for ordered particles as shown in Fig. 5c, and the structure factor is given by

$$S(Q) = \frac{1}{1 - w^2 - 2w \cos(Qd_m)} \quad (5)$$

where d_m corresponds to the average distance between HAP nanorods, and w is given with g -factor reflecting a distortion degree of the interparticle distance by

$$w = \exp\left(-\frac{1}{2}g^2d_m^2Q^2\right) \quad (6)$$

Fig. 7 shows the comparison of simulated profiles with equations (3) and (5), and observed ones, and fitting parameters are shown in Table 2. The simulated profiles are appropriate also at $Q < 0.025$ Å⁻¹. The peak position Q_{M1}

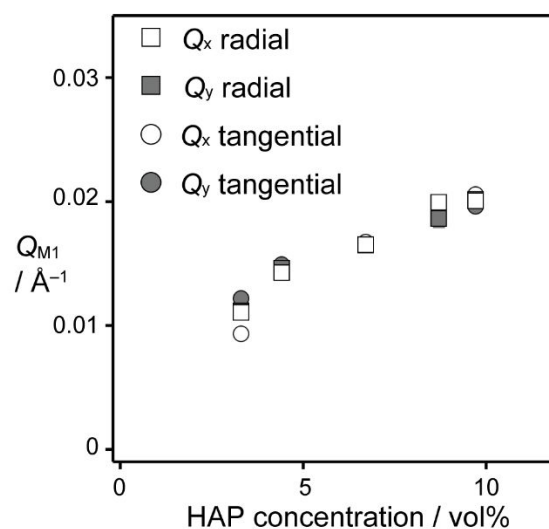


Fig. 9 Q_{M1} in radial and tangential sector-averaged SANS curves of HAP colloidal dispersions plotted as a function of various HAP concentrations.

depended mainly on d_m values, which were decreased with increasing the HAP concentration from 43 to 32 nm (Table 2). The simulated profiles with the model of the HAP/PAA core-shell structure with an ordered rod-particle model depicted as black line did not coincide with the observed results in the Q region 0.025 Å⁻¹–0.1 Å⁻¹ (Fig. 6 and 7). One possible explanation of this difference is that nanostructures of HAP-based composite nanorods caused a coherent scattering in this region. Detail observation for HAP nanorod structures with TEM revealed that HAP nanorod is not a single crystal but an assembly of nanocrystallites with 20–40 nm length and ca. 5 nm width (Fig. 2).¹³ Contribution of the nanostructures to coherent scattering was briefly estimated by using $P(Q)$ of a cylinder HAP crystal (Fig. 8a) with equation (3) and parameters

shown in Table 3. As shown in Fig. 8b, the simulated scattering profile for nanocrystalline cylinders coincides with the observed profile in the Q region $0.05\text{--}0.1 \text{ \AA}^{-1}$.

In that way, the peak position Q_{M1} linearly increased with increasing the concentration of the HAP nanorod dispersions, suggesting that the interparticle distance was decreased with increasing the concentration (Fig. 9 and Table 2). Estimated interparticle distance was in the range of 30 – 50 nm for the static HAP nanorod dispersions. The correlation between interparticle distance and HAP nanorod concentration was well agreed with our previous analyses with small-angle X-ray scattering⁵⁴. The consistency of LC behaviour and structures of HAP nanorod dispersions suggested that replacement of D_2O to H_2O did not significantly change the physical properties of HAP nanorod dispersions.

Shear-flow-induced ordering behaviour of HAP nanorods

Effects of mechanical shear force on the ordering of isotropic and LC HAP nanorod dispersions were evaluated with 2D radial and tangential SANS profiles (Fig. S2–S11) and sector-averaged SANS curves (Fig. S12–S16). At the HAP concentration of 3.3 vol%, 2D SANS profiles in both radial and tangential directions

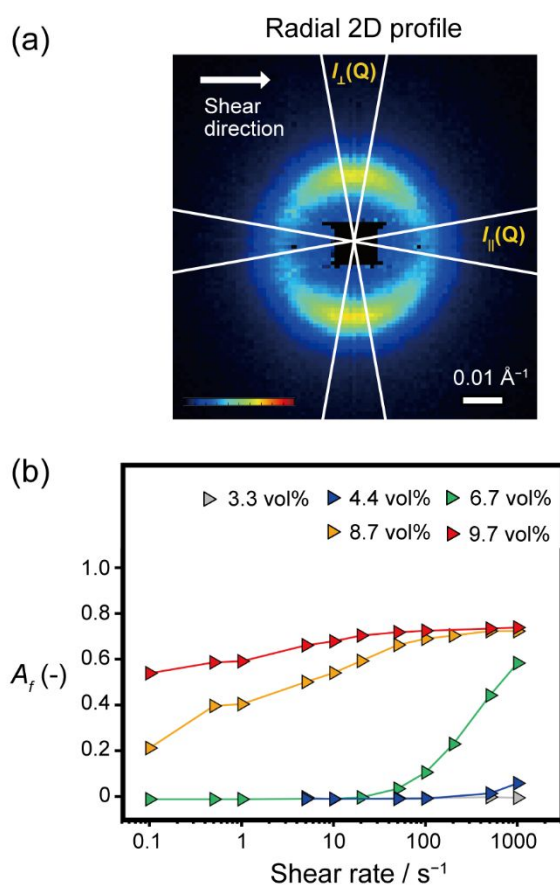


Fig. 10 (a) Representative radial 2D SANS profile of HAP nanorod dispersion with a shear force. (b) Alignment factor A_f of HAP nanorod dispersions plotted as a function of a variety of shear rates $0.1\text{--}1000 \text{ s}^{-1}$.

did not significantly change from ring spots up to the shear rate of 1000 s^{-1} (Fig. S2 and S3). From 4.4 to 9.7 vol%, 2D SANS

profiles in the radial direction became an anisotropic shape with increasing shear rates, suggesting shear-induced ordering of HAP nanorods (Fig. S4–S11). Orientation degrees A_f with mechanically shear force were estimated $I_{\perp}(Q)$ and $I_{\parallel}(Q)$ values, which are sector-averaged SANS curves perpendicular and parallel to the shear direction with the azimuthal angle of $\pm 10^\circ$, respectively (Fig. 10a).

$$A_f = \frac{\int_{Q_{min}}^{Q_{max}} I_{\perp}(Q) dQ - \int_{Q_{min}}^{Q_{max}} I_{\parallel}(Q) dQ}{\int_{Q_{min}}^{Q_{max}} I_{\perp}(Q) dQ + 2 \int_{Q_{min}}^{Q_{max}} I_{\parallel}(Q) dQ} \quad (7)$$

Q_{min} and Q_{max} values were set to appropriate values in the equation (7). Plots of orientation degree A_f of the HAP nanorod dispersions under a variety of shear rates are shown in Fig. 10b. $A_f > 0$ means the ordering of HAP nanorods in the shear flow direction, and the increasing onset of A_f values indicates the shear-induced phase transition from isotropic to nematic phases. HAP nanorods in dispersions at 4.4 and 6.7 vol% showed nematic ordering in shear flow, whereas these solutions were isotropic without mechanical shear force. The results suggested that HAP nanorod dispersions show shear-flow-induced transition from isotropic to nematic phases more than 4 vol%

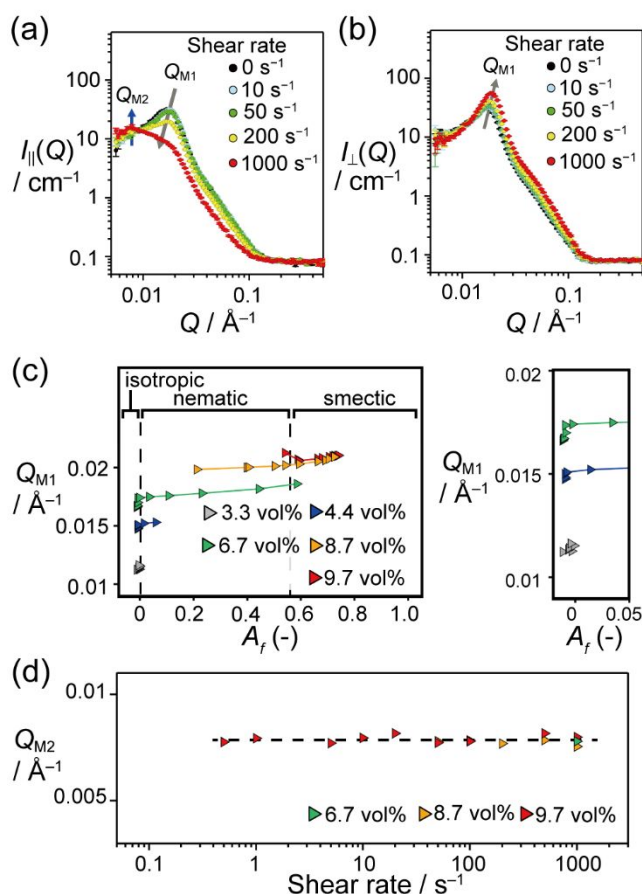


Fig. 11 (a,b) Sector-averaged SANS intensity curves of 6.7 vol% HAP nanorod dispersions in (a) parallel and (b) perpendicular to the shear direction, showing the profile change with increasing the shear rate up to 1000 s^{-1} . (c) Peak position Q_{M1}

plotted as a function of alignment factor A_r . Right part shows enlarged plots of an isotropic region. (d) Plots of Q_{M2} values in low- Q -region, suggesting layered ordering of HAP nanorods in the long-axis direction.

up to 1000 s^{-1} . In LC states of 8.7 and 9.7 vol% HAP nanorod dispersions, the unidirectional orientation was observed under mechanical shear force. As increasing the concentration, HAP dispersion was easier in the highly unidirectional orientation under the shear flow (Fig. 10b and Fig. S17).

Mechanical shear force also affected arrangements of HAP nanorods in dispersion states, not only their orientation. Typically, sector-averaged SANS curves of 6.7 vol% HAP are shown in Fig. 11. These sector-averaged SANS curves showed two distinct changes. One is the shift of Q_{M1} value, suggesting the change of the interparticle distance in the short-axis direction. In sector-averaged SANS curves perpendicular to the shear direction (Fig. 11b), the peaks around $Q = 0.017 \text{ \AA}^{-1}$ were shifted with the increase of the shear rate, suggesting that the shear force reduced the interparticle distance in the short-axis direction (Fig. S18). Correlation between orientation degree and the interparticle distance is shown in Fig. 11c. With slow shear rates to isotropic HAP dispersions, which did not align HAP nanorods, shear force also reduced interparticle distance in the short-axis direction (Fig. 11c, right part). Further increase of shear rates aligned the HAP nanorod particles, which is suggested from the change to anisotropic 2D SANS profiles. Increasing alignment degree of HAP nanorods decreased the excluded volume of HAP nanorods, resulting in decrease of interparticle distance.

The other is a peak emergence with higher shear rates more than 200 s^{-1} in a low- Q region of the parallel direction to the shear flow (Fig. 11a). Presumably, these peaks originated from interparticle distance in the long-axis direction. The peak position of the low- Q region was around 0.008 \AA^{-1} , corresponding to the d value *ca.* 80 nm, which is in agreement with our previous results of static SAXS measurements.⁵⁴ The peak position in the low- Q region, Q_{M2} was consistent against the change of the HAP nanorod concentration and applying shear rates (Fig. 11d), suggesting the formation of layered structures in HAP nanorod assemblies in the long-axis direction. The emergence of Q_{M2} peak with the increase of shear rates suggested that shear-flow-induced LC phase transitions from a nematic phase to a smectic-like phase with layered ordering. For 6.7 vol % of HAP nanorod dispersion, two phase transitions, isotropic to nematic then nematic to smectic-like phases, were observed with increasing shear rate up to 1000 s^{-1} . Although it is well known that shear treatment is one effective approach to the alignment control of LC materials,^{55–58} there are only few reports on shear-induced LC phase transition.^{59,60} The *in-situ* observation of the structural change under shear force unraveled uncommon phase transition behaviour of HAP nanorod dispersions.

All tangential 2D SANS profiles obtained under the shear force in the present study showed ring patterns (Fig. S2–S11). The results suggested that the HAP nanorods or their assemblies can freely rotate around the parallel axis to the shear flow up to the shear rate 1000 s^{-1} within the 1mm-gap

cell. The change of Q_{M1} values with concentration and shear rates was in similar trends to those values of the radial SANS profiles (Fig. S12–S17).

Dynamic viscosity of HAP nanorod dispersion

Evaluation of mechanical properties of HAP nanorod dispersions in isotropic, nematic and smectic phases is necessary for materials design of LC HAP dispersions for the application in structural materials. Fig. 12 shows dynamic viscosities of HAP nanorod dispersions under various shear rates with the phase diagram estimated with the SANS measurements. The isotropic states showed shear-thickening behaviour, whereas the LC states showed discontinuous change of dynamic viscosity in the range of $5\text{--}50 \text{ s}^{-1}$ and shear-thinning behaviour in the higher shear rates (Fig. S19 and S20).

This is the first time for the observation of shear-thickening and shear-thinning behaviour of colloidal LC materials involving phase transitions, therefore understanding of this mechanism is important for the design of mechanical responsive LC materials. One possible explanation about shear-thickening and shear-thinning behaviours of HAP LC nanorods is that there are competing effects on dynamic viscosity change, the enhancement of interparticle interactions causing shear-thickening, and alignment of HAP nanorods causing the shear-thinning. However, decrease of the dynamic viscosity change

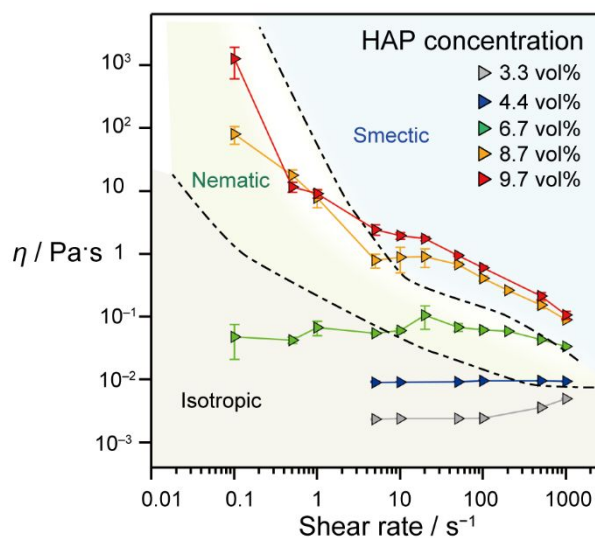


Fig. 12 Dynamic viscosities of HAP colloidal aqueous solutions plotted as a function of shear rates. Phase diagram estimated with structural analyses by SANS measurements is also depicted.

upon the nematic-smectic phase transition, where attractive interactions among particles were much enhanced, cannot be explained.

Another explanation is that the shear-thickening and shear-thinning behaviours arose from growing and disrupting nanorods assemblies, respectively. It is known that shear flow to the colloidal solutions induces both aggregation of colloidal particles and disruption of colloidal aggregation, resulting in

the increase or decrease of their dynamic viscosities, respectively,⁸ even what interaction drives aggregation of colloidal particles is not fully understood yet. The dynamic viscosities of colloidal solutions largely depend on domain size of colloidal aggregates.^{3,8,12} Hence, it is assumed that in the present study the shear-thickening behaviour was mainly caused by the formation of nanorod assembling domain accompanied by the enhancement of interparticle interactions, while the shear-thinning was caused by the disruption of HAP nanorod assemblies. For 6.7, 8.7 and 9.7 vol% HAP LC nanorod dispersions, discontinuous change of dynamic properties was observed around the shear rates $5 - 50 \text{ s}^{-1}$. In this region the shear flow simultaneously induced both assembling of colloidal HAP nanorods and disruption of their assemblies. On

the basis of combined results of the structural change and dynamic viscosity, promising effects of mechanical shear force on the ordering of HAP nanorods are schematically shown in Fig. 13. The major effect of mechanical shear force on the HAP nanorods is the decrease of interparticle distance. The interparticle distance was continuously decreased with increasing shear rate (Fig. S18). This might be caused by the interruption of free rotation of individual nanorods by shear force, resulting in the decrease of excluded volume of particles. Similarly, alignment degree of HAP nanorods was continuously increased (Fig. 10b). In contrary to the interparticle distance and the alignment degree, dynamic viscosity of HAP nanorod dispersion to the shear rate was not linearly changed (Fig. 12).

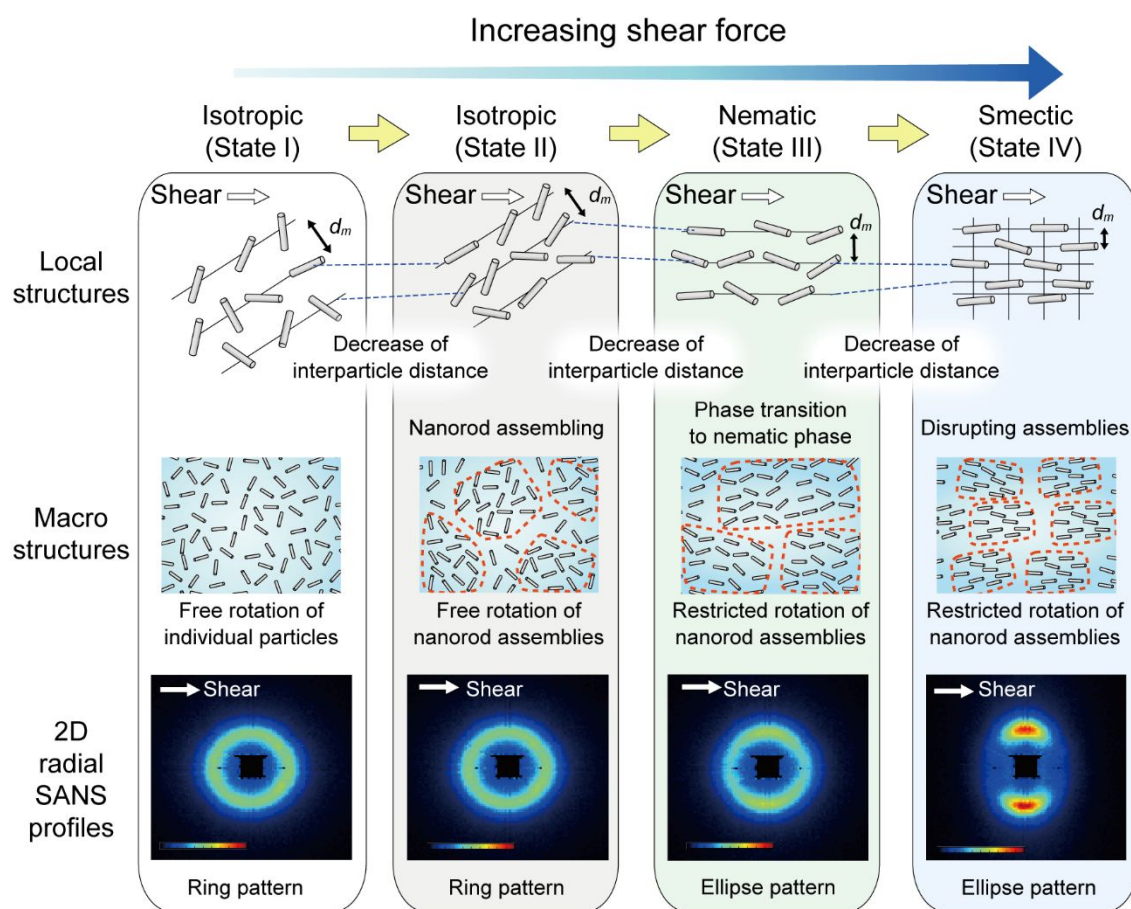


Fig. 13 Schematic illustration for proposed local and macroscopic structural change of HAP nanorods in D_2O dispersion by shear force. Shear force decreases the interparticle distance, leading to the formation of nanorod assemblies. In low concentrations and low shear rates, nanorod assemblies can freely rotate in the isotropic dispersion (State II). Increase of the shear rate restricts rotation of nanorod assemblies, resulting in the phase transition from isotropic to nematic phases (State III). In high concentrations and high shear rates, the HAP nanorod dispersions transits to a smectic-like phase with layered ordering in the long-axis direction (State IV).

It is noteworthy that dynamic viscosity was increased before the nanorod alignment, suggesting that HAP nanorods assembled by the shear force in isotropic colloidal dispersions. Discontinuous change of dynamic viscosity in the region where the orientation degree was increasing, and shear-thinning region at higher shear rates involving the nematic-smectic phase transition strongly suggested that domain size of HAP

nanorod assemblies dominated the dynamic viscosity, rather than the interactions among HAP nanorods playing a minor role in the change of dynamic viscosity. Under the assumption that the shear-thickening behaviour of isotropic HAP nanorod dispersions under low shear rates was caused by growing HAP nanorod assemblies (Fig. 13, state II), HAP nanorods were unidirectionally aligned by the shear flow after growing

domain to a sufficient size. As growing the domain, its Brownian motion was suppressed. In this manner, free rotation of growing HAP nanorod domains was inhibited by the shear flow, resulting in the alignment of the domains (Fig. 13, state III). Note that entropic interactions may exist the domains and competes or cooperates with other interactions to form aligned nanorod assemblies. Thus, shear force cooperatively worked with interparticle interactions on ordering of HAP colloidal nanorods. Further alignment by the shear force decreased the excluded volume of nanorods, leading to formation of a more-packed structure of nanorods schematically shown as state IV in Fig. 13.

Present observations are consistent with previous reports on ordering behaviour of LC materials based on subnano- to submicro-scaled units by external fields, showing LC phases have much higher responsivities than their isotropic phases.^{13,61,62} These properties might be attributable to decreased free motion of LC molecules or particles that form a large-sized domain. Unfortunately, understanding about ordering behaviour of HAP nanorod dispersions under shear force has not been completed. Rheo-SANS measurements of HAP nanorod dispersions with *ca.* 100 nm length and *ca.* 20 nm width suggested the possibility that particle assemblies play important roles in external-stimuli responsivity. Observation for size and morphological dependence of ordering behaviour of anisotropic colloidal particles is important for further understanding of the effects of shear force on the structural change of colloidal dispersions, as well as computational studies on flow behaviour of colloidal dispersions.

Conclusions

Rheo-SANS measurements shed light on shear-induced LC phase transitions of HAP-based nanorod dispersions involving with the discontinuous change of their rheological properties. The analyses of structural and viscosity changes suggested that three kinds of effects of shear flow on ordered structures of HAP-based nanorod dispersions; the enhancement of interparticle interactions, alignment of HAP nanorods to the shear flow direction, and formation and disruption of colloidal assembling of HAP nanorods. Considering both of dynamic viscosity and local structural changes of HAP nanorod dispersions, the shear flow cannot independently align the HAP nanorods with *ca.* 100 nm length and *ca.* 20 nm width by the restriction of their Brownian motion, but it cooperatively works with the interparticle interactions between nanorods, for example entropic interactions, in the alignment of nanorod particles. Colloidal HAP nanorods showed a distinctive shear-thickening behaviour observed through the phase transition from isotropic to LC phases, which would be utilized in shear-responsive mechanical materials. And high shear rates to the HAP nanorod dispersions induced highly ordered structures with a unidirectional orientation with the disruption of nanorod assemblies causing shear-thinning. This feature may be an advantage of shear force for the orientational control of

high viscous materials, in comparison of other external stimuli of electric and magnetic fields.

The definition of interparticle interactions is necessary to fully understand of the ordering behaviour of nanorod particles in isotropic and LC dispersions. In the present study, SANS profiles of HAP nanorod dispersions in dense states cannot be fitted with simulated curves only with the Hayter-Penfold model for randomly-oriented rod particles because the interparticle interaction between HAP nanorod composites contains many forces across multiple length scales, for example, electrostatic repulsion force, van der Waals interactions, hydrodynamic interactions, and entropic interaction etc. However, Rheo-SANS measurements of LC materials have a large potential for providing fundamental insights for the interparticle interactions among anisotropic colloidal particles because they can provide structural information of highly oriented particles in three-dimensional geometries. The interactions among colloidal particles largely depend on size, morphology and aspect ratio of colloidal particles, thereby Rheo-SANS measurements of morphologically controlled colloidal LC materials will provide significant information leading to the materials design towards shear-responsive LC materials. In addition, combination with theoretical calculation for the interparticle interactions would also help us to understand ordering behaviour of LC materials with external stimuli.

Conflicts of interest

There are no conflicts to declare.

Acknowledgements

This study was partially supported by KAKENHI Grant No. JP19H05715, JP19H05717 (Grant-in-Aid for Scientific Research on Innovative Area: Aquatic Functional Materials), and CREST, JST (JPMJCR15Q3). Rheo-SANS measurements were performed with the approval of the Neutron Program Review Committee (Proposal No. 2018B0264). The authors would like to thank Nanotechnology Platform at the University of Tokyo for TEM observation.

References

- 1 *Colloids and Colloid Assemblies*, ed. F. Caruso, Wiley-VCH, Weinheim, 2003.
- 2 R. G. Larson, *The Structure and Rheology of Complex Fluids*, Oxford University Press, New York, 1999.
- 3 X. Cheng, J. H. McCoy, J. N. Israelachvili and I. Cohen, *Science*, 2011, **333**, 1276–1279.
- 4 M. Siebenbürger, M. Fuchs and M. Ballauff, *Soft Matter*, 2012, **8**, 4104–4024.
- 5 S. Pednekar, J. Chun and J. F. Morris, *Soft Matter*, 2017, **13**, 1773–1779.
- 6 N. M. James, E. Han, R. A. L. de la Cruz, J. Jureller and H. M. Jaeger, *Nat. Mater.*, 2018, **17**, 965–970.
- 7 C.-P. Hsu, S. N. Ramakrishna, M. Zanini, N. D. Spencer and L. Isa, *Proc. Natl. Acad. Sci. USA*, 2018, **115**, 5117–5122.
- 8 K. Ueno, *Polym. J.*, 2018, **50**, 951–958.

- 9 R. Mhanna, J. Lee, S. Narayanan, D. H. Reich and R. L. Leheny, *Nanoscale*, 2019, **11**, 7875–7884.
- 10 Y. Ye, H. Xiao, K. Reaves, B. McCulloch, J. F. Mike and J. L. Lutkenhaus, *ACS Appl. Nano Mater.*, 2018, **1**, 2774–2884.
- 11 M. De Corato and G. Natale, *Macromolecules*, 2019, **52**, 4907–4915.
- 12 J. T. Stimatze, D. A. Egolf and J. S. Urbach, *Soft Matter*, 2016, **12**, 7764–7771.
- 13 M. Nakayama, S. Kajiyama, A. Kumamoto, T. Nishimura, Y. Ikuhara, M. Yamato and T. Kato, *Nat. Commun.*, 2018, **9**, 568.
- 14 M. Nakayama, S. Kajiyama, T. Nishimura and T. Kato, *Chem. Sci.*, 2015, **6**, 6230–6234.
- 15 A. Dessombz, D. Chiche, P. Davidson, P. Panine, C. Chanéac and J.-P. Jolivet, *J. Am. Chem. Soc.*, 2007, **129**, 5904–5909.
- 16 J. Kim, S. Michelin, M. Hilbers, L. Martinelli, E. Chaudan, G. Amselem, E. Fradet, J.-P. Boilot, A. M. Brouwer, C. N. Baroud, J. Peretti and T. Gacoin, *Nat. Nanotech.*, 2017, **12**, 914–919.
- 17 M. Aizadehgiashi, A. Khabibullin, Y. Li, E. Prince, M. Abolhasani and E. Kumacheva, *Langmuir*, 2018, **34**, 322–330.
- 18 X. Liu, G. Qi, A. M. G. Park, A. Rodriguez-Gonzalez, A. Enotiadis, W. Pan, V. Kosma, G. D. Fuchs, B. J. Kirby and E. P. Giannelis, *Small*, 2019, **15**, 1901666.
- 19 T. Sawada, Y. Murata, H. Marubayashi, S. Nojima, J. Morikawa and T. Serizawa, *Sci. Rep.*, 2018, **8**, 5412.
- 20 M. Grezelczak, J. Vermant, E. M. Furst and L. M. Liz-Marzán, *ACS Nano*, 2010, **4**, 3591–3605.
- 21 M. Nakayama, W. Q. Lim, S. Kajiyama, A. Kumamoto, Y. Ikuhara, T. Kato and Y. Zhao, *ACS Appl. Mater. Interfaces*, 2019, **11**, 17759–17765.
- 22 F. Kimura, T. Kimura, M. Tamura, A. Hirai, M. Ikuno and F. Horii, *Langmuir* 2005, **21**, 2034–2037.
- 23 M. Wang, L. He, S. Zorba and Y. Yin, *Nano Lett.*, 2014, **14**, 3966–3971.
- 24 P. P. Donahue, C. Zhang, N. Nye, J. Miller, C.-Y. Wang, R. Tang, C. Christodoulides, C. D. Keating and Z. Liu, *ACS Nano*, 2018, **12**, 7343–7351.
- 25 T. Nakato, A. Takahashi, S. Terada, S. Yamaguchi, E. Mouri, M. Shintate, S. Yamamoto, Y. Yamauchi and N. Miyamoto, *Langmuir*, 2019, **35**, 14543–14552.
- 26 Y. Wang, Y. Zheng, L. Sheng, J. Zhao and Y. Li, *Nanoscale*, 2020, **12**, 1374–1383.
- 27 B. Klöckner, P. Daniel, M. Brehmer, W. Tremel and R. Zentel, *J. Mater. Chem. C*, 2017, **5**, 6688–6696.
- 28 K. Usami and A. Okamoto, *Org. Biomol. Chem.*, 2017, **15**, 8888–8893.
- 29 S. Campisi, C. Castellano and A. Gervasini, *New J. Chem.*, 2018, **42**, 4520–4530.
- 30 L. K. Grunenfelder, S. Herrera and D. Kisailus, *Small*, 2014, **10**, 3207–3232.
- 31 J. Fu, X. Liu, L. Tan, Z. Cui, Y. Zheng, Y. Liang, Z. Li, S. Zhu, K. Wai, K. Yeung, X. Feng, X. Wang and S. Wu, *ACS Nano*, 2019, **13**, 13581–13594.
- 32 M. Yashima, N. Kubo, K. Omoto, H. Fujimori, K. Fujii and K. Ohoyama, *J. Phys. Chem. C*, 2014, **118**, 5180–5187.
- 33 X. Zhang and M. Z. Yates, *ACS Appl. Mater. Interfaces*, 2018, **10**, 17232–17239.
- 34 S. Kajiyama, T. Sakamoto, M. Inoue, T. Nishimura, T. Yokoi, C. Ohtsuki and T. Kato, *CrystEngComm*, 2016, **18**, 8388–8395.
- 35 R. Ichikawa, S. Kajiyama, M. Iimura and T. Kato, *Langmuir*, 2019, **35**, 4077–4084.
- 36 S. Chen, M. Krumova, H. Cölfen and E. V. Sturm, *Chem. Mater.*, 2019, **31**, 1543–1551.
- 37 K. Aita, Y. Oaki, C. Ohtsuki and H. Imai, *CrystEngComm*, 2015, **17**, 5551–5555.
- 38 M. Kusunoki, Y. Sakoishi, T. Makino, T. Tsunemine, N. Fujita, Y. Okada, D. Okai, H. Togo and T. Hayami, *Appl. Surf. Sci.*, 2019, **484**, 433–440.
- 39 F. Peng, M. T. Shaw, J. R. Olson and M. Wei, *J. Phys. Chem. C*, 2011, **115**, 15743–15751.
- 40 Y. Kawabata, R. Bradbury, S. Kugizaki, K. Weigandt, Y. B. Melnichenko, K. Sadakane, N. L. Yamada, H. Endo, M. Nagao and H. Seto, *J. Chem. Phys.*, 2017, **147**, 034905.
- 41 T. Matsunaga, H. Endo, M. Takeda and M. Shibayama, *Macromolecules*, 2010, **43**, 5075–5082.
- 42 F. Chu, N. Heptner, Y. Lu, M. Siebenbürger, P. Lindner, J. Dzubiella and M. Ballauff, *Langmuir*, 2015, **32**, 5992–6000.
- 43 M. Takeda, T. Kusano, T. Matsunaga, H. Endo, M. Shibayama and T. Shikata, *Langmuir*, 2011, **27**, 1731–1738.
- 44 I. W. Hamley, S. Burholt, J. Hutchinson, V. Castelletto, E. R. da Silva, W. Alves, P. Gutfreund, L. Porcar, R. Dattani, D. Hermida-Merino, G. Newby, M. Reza, J. Ruokolainen and J. Stasiak, *Biomacromolecules*, 2017, **18**, 141–149.
- 45 V. T. Kelleppan, J. E. Moore, T. M. McCoy, A. V. Sokolova, L. de Campo, B. L. Wilkinson and R. F. Tabor, *Langmuir*, 2018, **34**, 970–977.
- 46 H. Iwase, R. Kawai, K. Morishima, S. Takata, T. Yoshimura and M. Shibayama, *J. Colloids Interfaces*, 2019, **538**, 357–366.
- 47 F. Zhang, J. Ilavsky, G. G. Long, J. P. G. Quintana, A. J. Allen and P. R. Jemian, *Metall. Mater. Trans. A*, 2010, **41**, 1151–1158.
- 48 J. B. Hayter and J. Penfold, *Mol. Phys.*, 1981, **42**, 109–118.
- 49 C. J. S. Ibsen, D. Chernyshov and H. Birkedal, *Chem. Eur. J.*, 2016, **22**, 12347–12357.
- 50 S. Sun, L.-B. Mao, Z. Lei, S.-H. Yu and H. Cölfen, *Angew. Chem. Int. Ed.*, 2016, **55**, 11765–11769.
- 51 P. Mandal, S. Maji, S. Panja, O. P. Bajpai, T. K. Maiti and S. Chattopadhyay, *New J. Chem.*, 2019, **43**, 3026–3037.
- 52 C. Xiao, M. Li, B. Wang, M.-F. Liu, C. Shao, H. Pan, Y. Lu, B.-B. Xu, S. Li, D. Zhan, Y. Jiang, R. Tang, X. Y. Liu and H. Cölfen, *Nat. Commun.*, 2017, **8**, 1398.
- 53 M. Bergström, J. S. Pedersen, P. Schurtenberger and S. U. Egelhaaf, *J. Phys. Chem. B*, 1999, **103**, 9888–9897.
- 54 T. Hoshino, M. Nakayama, S. Fujinami, T. Nakatani, Y. Kohmura and T. Kato, *Soft Matter*, 2019, **15**, 3315–3322.
- 55 T. Ichikawa, T. Kato and H. Ohno, *Chem. Commun.*, 2019, **55**, 8205–8214.
- 56 W. R. Burghardt, *Macromol. Chem. Phys.*, 1998, **199**, 471–488.
- 57 M. Yoshio, T. Mukai, H. Ohno and T. Kato, *J. Am. Chem. Soc.*, 2004, **126**, 994–995.
- 58 I. Wurzbach, C. Rothe, K. Bruchlos, S. Ludwigs and F. Giesselmann, *J. Mater. Chem. C*, 2019, **7**, 2615–2624.
- 59 Y. Sagara and T. Kato, *Angew. Chem. Int. Ed.*, 2008, **47**, 5175–5178.
- 60 B. Medronho, S. Shafaei, R. Szopko, M. G. Miguel, U. Olsson and C. Schmidt, *Langmuir*, 2008, **24**, 6480–6486.
- 61 X. Feng, M. E. Tousley, M. G. Cowan, B. R. Wiesenauer, S. Nejati, Y. Choo, R. D. Noble, M. Elimelech, D. L. Gin and C. O. Osuji, *ACS Nano*, 2014, **8**, 11977–11986.
- 62 Y. Mao, M. Bleuel, Y. Lyu, X. Zhang, D. Henderson, H. Wang and R. M. Briber, *Langmuir*, 2018, **34**, 8042–8051.

Table of Contents

Shear-induced structural changes and phase transition behaviour of colloidal hydroxyapatite-based nanorod composites are observed with *in-situ* small-angle neutron scattering and rheological measurements.

